Unusually long path length for a nearly scatter-free solar particle event observed by Solar Orbiter at 0.43 au

Robert F. Wimmer-Schweingruber[1], Lars Berger[1], Alexander Kollhoff[1], Patrick Kühl[1], Bernd Heber[1], Liu Yang[1], Verena Heidrich-Meisner[1], Andreas Klassen[1], Raúl Gomez-Herrero[2], Javier Rodriguez-Pacheco[2], George C. Ho[3], Glenn M. Mason[3], Nils P. Janitzek[4,5], Athanasios Kouloumvakos[3], Linghua Wang[6], Alexander Warmuth[7], David Lario[8], Fernando Carcaboso[8,9], Christopher J. Owen[10], Radoslav Bučík[11], Daniel Pacheco[1], Olga Malandraki[12], Robert C. Allen[3], Luciano Rodriguez[13], Daria Shukhobodskaia[13], Francisco Espinosa Lara[2], Ignacio Cernuda[2], Stephan I. Böttcher[1], Sandra Eldrum[1], Sebastian Fleth[1], and Zigong Xu[1]

[1] Institute of Experimental and Applied Physics, Christian-Albrechts-University Kiel, Leibnizstraße 11, 24118 Kiel, Germany
e-mail: wimmer@physik.uni-kiel.de
[2] Universidad de Alcalá, Space Research Group (SRG-UAH), Plaza de San Diego s/n, 28801 Alcalá de Henares, Madrid, Spain
[3] Johns Hopkins University Applied Physics Laboratory, 11100 Johns Hopkins Rd, Laurel, MD 20723, USA
[4] Physikalisch-Meteorologisches Observatorium Davos/World Radiation Center, Dorfstrasse 33, 7260 Davos Dorf, Switzerland
[5] Institut für Teilchenphysik und Astrophysik, Eidgenössische Technische Hochschule Zürich, Wolfgang-Pauli-Str. 27, 8093 Zürich, Switzerland
[6] School of Earth and Space Sciences, No. 2 Yifu Building, Peking University, No.5 Yiheyuan Road, Haidian District, Beijing 100871, PR China
[7] Leibniz-Institut für Astrophysik Potsdam (AIP), An der Sternwarte 16, 14482 Potsdam, Germany
[8] NASA Goddard Space Flight Center, Heliophysics Science Division, Mail code 672, Greenbelt, MD 20771, USA
[9] Department of Physics, The Catholic University of America, 620 Michigan Ave., N.E. Washington, DC 20064, USA
[10] Mullard Space Science Laboratory, University College London, Holmbury St. Mary, Dorking, Surrey RH5 6NT, UK
[11] Southwest Research Institute, 6220 Culebra Road, San Antonio, TX 78238, USA
[12] National Observatory of Athens, Institute for Astronomy, Astrophysics, Space Applications and Remote Sensing (IAASARS), Vas. Pavlou & I. Metaxa, GR-15 236 Penteli, Greece
[13] Solar-Terrestrial Centre of Excellence – SIDC, Royal Observatory of Belgium, Ringlaan -3- Av. Circulaire, 1180 Brussels, Belgium

ABSTRACT

Context. After their acceleration and release at the Sun, solar energetic particles (SEPs) are injected into the interplanetary medium and are bound to the interplanetary magnetic field (IMF) by the Lorentz force. The expansion of the IMF close to the Sun focuses the particle pitch-angle distribution, and scattering counteracts this focusing. Solar Orbiter observed an unusual solar particle event on 9 April 2022 when it was at 0.43 astronomical units (au) from the Sun.
Aims. We show that the inferred IMF along which the SEPs traveled was about three times longer than the nominal length of the Parker spiral and provide an explanation for this apparently long path.
Methods. We used velocity dispersion analysis (VDA) information to infer the spiral length along which the electrons and ions traveled and infer their solar release times and arrival direction.
Results. The path length inferred from VDA is approximately three times longer than the nominal Parker spiral. Nevertheless, the pitch-angle distribution of the particles of this event is highly anisotropic, and the electrons and ions appear to be streaming along the same IMF structures. The angular width of the streaming population is estimated to be approximately 30 degrees. The highly anisotropic ion beam was observed for more than 12 h. This may be due to the low level of fluctuations in the IMF, which in turn is very probably due to this event being inside an interplanetary coronal mass ejection The slow and small rotation in the IMF suggests a flux-rope structure. Small flux dropouts are associated with very small changes in pitch angle, which may be explained by different flux tubes connecting to different locations in the flare region.
Conclusions. The unusually long path length along which the electrons and ions have propagated virtually scatter-free together with the short-term flux dropouts offer excellent opportunities to study the transport of SEPs within interplanetary structures. The 9 April 2022 solar particle event offers an especially rich number of unique observations that can be used to limit SEP transport models.

Key words. Sun: flares – Sun: coronal mass ejections (CMEs) – Sun: activity – Sun: particle emission

1. Introduction

Solar particle events originate in association with solar flares and/or coronal shocks driven by coronal mass ejections (CMEs). Electrons escaping from the acceleration region excite Langmuir waves as they propagate from the solar corona to interplanetary space, which can be subsequently converted into type III radio emission (Wang et al. 2012). It is well known that impulsive electron events are associated with type III radio bursts and generally are also ^{3}He-rich (Reames et al. 1985; Reames & Stone 1986).

As the solar energetic particles (SEPs), be they electrons or ions, propagate outward through the interplanetary medium, their pitch-angle distribution is affected by focusing due to the expanding magnetic field and scattering off irregularities in the interplanetary magnetic field (IMF). Zhao et al. (2019) performed a statistical analysis of the IMF path lengths of 81 solar energetic electron events observed by Wind between 1994 and 2016 using velocity dispersion analysis (VDA) and a modified version thereof. They found consistent results for all methods and average IMF spiral lengths that agree well with the average length of the Parker spiral with little field-line meandering. This in turn limits the amount of scattering undergone by the particles on their way from the Sun to the observer (Laitinen et al. 2015). In the case of observers at 1 astronomical unit (au), scattering can appear to lengthen the inferred spiral length (Laitinen & Dalla 2019). Closer to the Sun than the usual 1 au, we expect more scattering because the fluctuations in the IMF are larger, but also a stronger effect of focusing. The combined effects of scattering and focusing are treated by so-called focused-transport models; van den Berg et al. (2020) provide an up-to-date review of the topic.

The situation can be much more complicated when the observer is embedded in an interplanetary coronal mass ejection (ICME) because the magnetic configuration of ICMEs is much more complex than the standard Parker spiral. The energetic particles we investigate here are tied to such a large-scale magnetic field. The low level of turbulence inside ICMEs strongly limits pitch-angle diffusion. Several authors have investigated energetic particle transport and observations inside ICMEs (e.g., Torsti et al. 2004; Tan et al. 2013; Leske et al. 2012; Gómez-Herrero et al. 2017), with mixed results as to the length of the IMF line connecting the source region and the observer. To our knowledge, only the observations reported by Gómez-Herrero et al. (2017) show a comparable ratio of path length to distance to the Sun to the one reported here.

Solar Orbiter, a mission of international cooperation between the European Space Agency (ESA) and the US National Aeronautics and Space Administration (NASA; Müller et al. 2020), has been exploring the inner heliosphere since its launch on 10 February 2020. On 26 March 2022, it reached perihelion at 0.32 au, which offered an exciting glimpse of the physics of the inner heliosphere with Solar Orbiter's complement of ten sophisticated science instruments. Here we use data from five instruments to investigate a virtually scatter-free solar particle event with an unusually long IMF path length. These observations provide strong limits on the effects of scattering and focusing of energetic particles in the inner heliosphere. A similar, virtually scatter-free event that occurred when Solar Orbiter was at 0.95 au was studied by Ho et al. (2022); here we discuss observations at 0.43 au. Those authors found that the observations of flux dropouts across multiple injections of solar particle events imply that field-line random walk at 1 au still maintains its magnetic connection to a small region back at the Sun.

In the next section we describe the data used for our study and give an overview of the 9 April 2022 events before we explain our analysis in Sect. 3. We discuss our results in Sect. 4, interpret them in Sect. 5, and present our conclusions in Sect. 6.

2. Data

We used data from the Electron Proton Telescope (EPT), which is one of the sensors of the Energetic Particle Detector (EPD) suite on Solar Orbiter (Rodríguez-Pacheco et al. 2020; Wimmer-Schweingruber et al. 2021). It discriminates ions
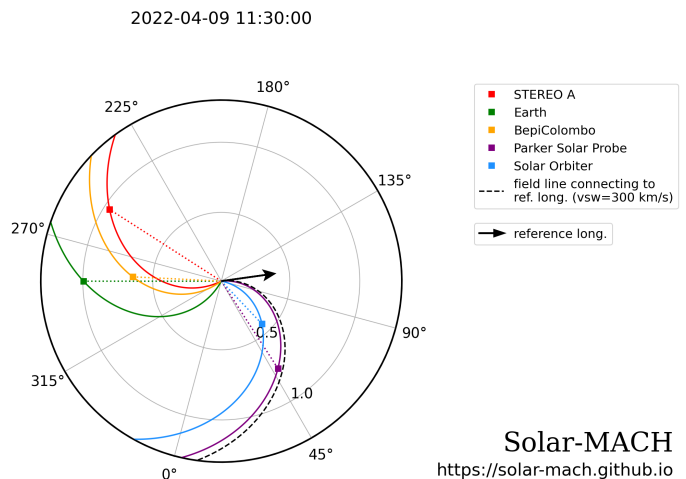
2022-04-09 11:30:00

Fig. 1. Overview of locations of spacecraft in the inner heliosphere and their nominal Parker spiral connections back to the Sun. Solar Orbiter is shown in blue, PSP in purple, STEREO-A in red, BepiColombo in orange, and Earth assets in green on 9 April 2022 in Carrington longitude. The arrow indicates the approximate source longitude of the event studied in this paper. From Solar MACH (Gieseler et al. 2023).

from electrons using the foil-magnet technique, very similar to the Solar Electron Proton Telescope (SEPT) instrument (Müller-Mellin et al. 2008) on the Solar TErrestrial RElations Observatory (STEREO) mission (Kaiser et al. 2008). EPT measures ions from ~25–6400 keV and electrons between ~25–474 keV. EPT consists of two double-ended units that point in four directions: Sun, anti-Sun, north, and south. Their circular field of view (FoV) has a half opening angle of 15°, their pointing directions (as well as those of the other EPD sensors) are given in Table A.1. We also used data from the High-Energy Telescope (HET) of EPD, which points in the same directions as EPT, but covers ion energies up to 100 MeV nuc^{-1} (protons) and 20 MeV for electrons. In addition, we also show data from the EPD Suprathermal Ion Spectrograph (SIS), which uses time-of-flight and residual energy measurements to determine the ion composition from 0.1–10 MeV nuc^{-1}. Furthermore, we use data from the magnetometer (MAG) on Solar Orbiter (Horbury et al. 2020) to determine pitch-angle distributions, of the Proton-Alpha Sensor (PAS) and the Electrostatic Analyser System (EAS) of the Solar Wind Analyzer (SWA; Owen et al. 2020), the Spectrometer/Telescope for Imaging X-rays (STIX; Krucker et al. 2020) to relate EPD measurements to X-ray flares, and the Full Disk Imager (FSI) of the Extreme Ultraviolet Imager (EUI; Rochus et al. 2020) provides context images of the solar source.

The source region of the 9 April 2022 solar particle event was not visible from Earth. This can be seen in Fig. 1, which shows the positions of spacecraft in the inner heliosphere (i.e., within ~1 au in the Carrington longitude system) Solar Orbiter and Parker Solar Probe (PSP) were to the west of the Sun as seen from Earth, both with a nominal magnetic connection to the Sun nearly 180 degrees opposite from the Earth. Nominal Parker spirals were drawn for 400 km s^{-1} solar wind speed for Earth, BepiColombo, and STEREO-A, but 300 km s^{-1} for Solar Orbiter and PSP. We will see later on that this was the solar wind speed observed at Solar Orbiter during this period of time. The approximate source longitude of the event studied here is indicated by the right-pointing arrow.
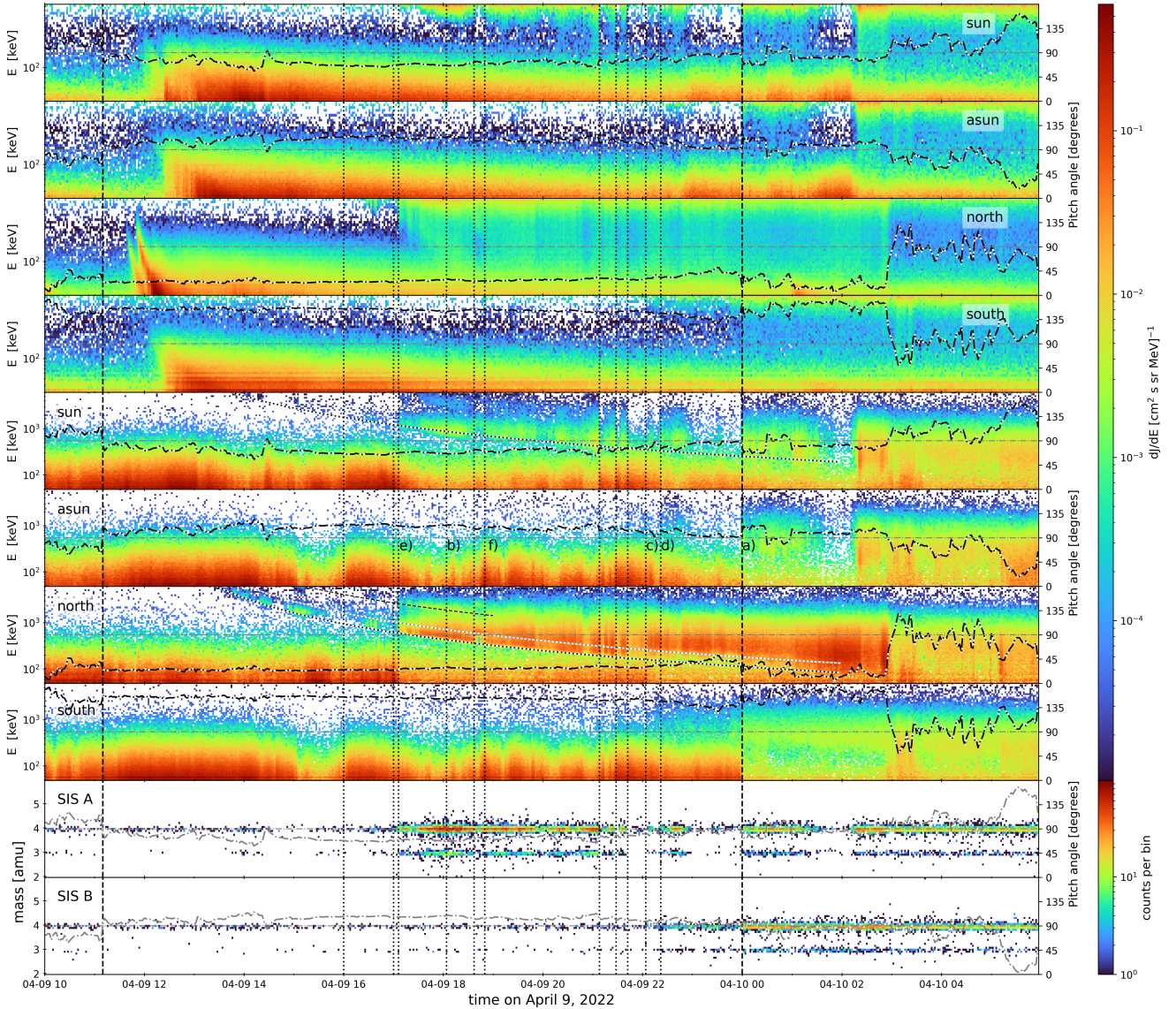
Fig. 2. Time series of observations at Solar Orbiter I. The top four panels show EPT foil observations from different telescopes, as indicated in the upper-right corner of each panel. Pitch angle is also shown as a dot-dashed line; its scale is shown on the right-hand axis. The next four panels from the top show observations in the EPT magnet channel by telescope, as indicated in the upper-left corner of each panel, as well as pitch angle, as in the previous panels. The slanted dotted and dashed curves show the earliest ion onsets as seen by the Sun and north telescopes and as determined in Sect. 3. It is obvious that the north telescope sees the highest flux, which in itself is a clear indication of an anisotropic flow. The two bottom panels show counts of helium isotopes as measured by SIS between 0.5 and 2.0 MeV nuc^{-1}, with the central pitch angles shown as a dash-dotted gray line. The vertical dotted lines and annotations (a)–(f) are discussed in Sect. 4, as are the thick vertical dashed lines. They mark the onset and end of a time period with very low Alfvénic Mach number in which this event is embedded.

Figure 2 shows data from EPT, SIS, and MAG from 9 April 2022, 10:00 UT to 10 April 2022, 06:00 UT. We note that all times are given as UT in the following and that we therefore do not repeat this information. Primary particle energy is shown on the left-hand y axis, time on the x-axis, and differential flux is color coded. The top four panels show differential fluxes of electrons measured by the four EPT apertures (i.e., Sun, anti-Sun, north, and south), the next four panels those for ions. The bottom two panels show SIS count rates of the helium isotopes as a function of time for the sunward-pointing SIS A and the nearly anti-Sun-pointing SIS B telescopes. The dash-dotted line in each of the panels shows the central pitch angle for the individual telescopes, the values are shown on the right-hand y-axis, a faint dash-dotted line at 90 degrees has been added for reference.

The slanted dotted curve shown for the Sun telescope and the two dotted and the dashed curves for the north telescope in Fig. 2 give the result of the VDA performed for protons (dotted) and helium (dashed) from which solar release times and path lengths of the IMF of the particle event can be derived as is discussed in Sect. 3[1]. The vertical dotted lines serve to guide the eye and are explained in more detail below as well as in Sects. 3 and 4, as are annotations (a)–(f) in Figs. 2 and 3. The large values for the differential ion fluxes at low energies ($\lesssim 200$ keV) are unrelated to the solar particle event studied here but due to a variable population of suprathermal and low-energy particles.

---

[1] EPT data are shown using the energy ranges obtained from proton calibrations, which are too low for helium. At the same speed helium loses more energy in the detector's dead layer than protons.
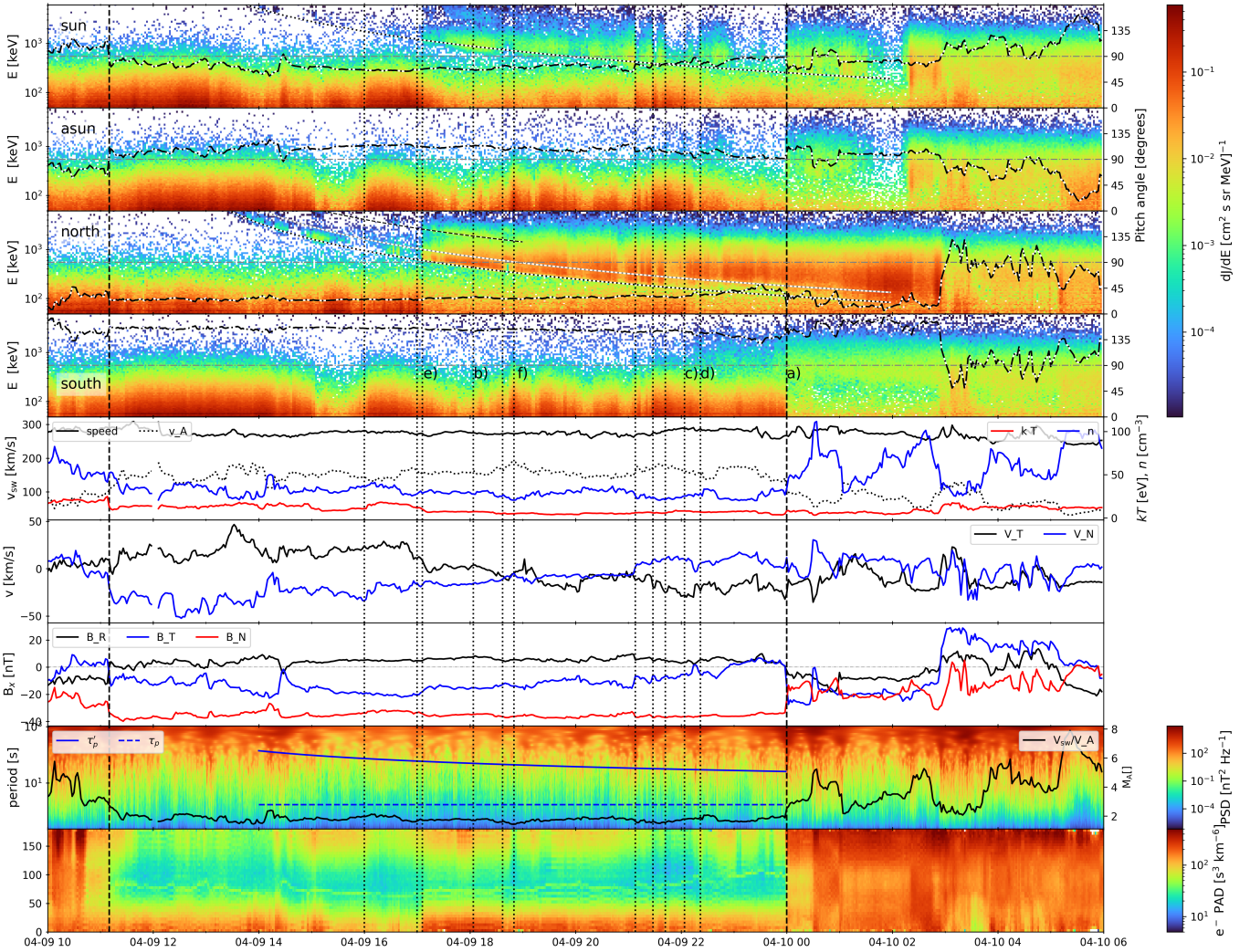
Fig. 3. Time series of observations at Solar Orbiter II. The top four panels show EPT magnet channel observations by telescope repeated from Fig. 2. Vertical dashed and dotted lines and annotations are repeated from that figure for easier comparison, as are the dashed and dotted VDA curves for helium ions and protons. The fifth panel from the top shows solar wind bulk speed (black), Alfvén speed (dotted black), temperature (red, right-hand axis), and density (blue, right-hand axis). The sixth panel shows tangential (T) and normal (N) components of the bulk velocity, and the seventh shows IMF data in RTN coordinates. A horizontal, thin, dash-dotted gray line has been added to indicate 0 nT. The seventh panel shows the power spectral density of the fluctuations in the IMF, as well as the approximate proton gyro-period in the solar wind rest frame (dashed line) and the period at which energetic protons are in first-order cyclotron resonance (solid line). The solid black line shows the Alfvénic Mach number (M_A, right-hand axis). The bottom panel shows the 70 eV electron pitch-angle distribution as measured by SWA.

Occasionally, these low-energy ions indicate that Solar Orbiter enters a different plasma regime, for instance around 00:00 on 10 April (annotation a in Figs. 2 and 3) when this flux of suprathermal ions is greatly diminished in the south telescope.

The most prominent feature in the electron measurements (top four panels in Fig. 2) is the double injection of electrons seen just before ~12:00 on 9 April in the north telescope. It is followed by an increase in near-relativistic electrons in all other telescopes about half an hour later (more timing information is given in Sects. 3 and 4). Around 17:00 of 9 April, high-energy (~1 MeV) ions can be seen in the Sun and north telescopes. These ions have enough energy to penetrate the thin polyimide layer that is deposited on the solid-state detectors of the "foil" side of EPT and thus contaminate the electron signal. Nevertheless, early on in the particle event, electrons are measured cleanly because ~1 MeV ions are much slower and arrive later. The two electron events are shown in more detail in Fig. 7 and discussed in Sect. 3.

Figure 3 repeats the EPT ion observations in the top four panels just as they were shown in Fig. 2 but adds solar wind measurements in the lower panels for comparison. The north telescope shows clear injections of ions about two hours later than the electron injections (shown in Fig. 2), which is also seen in the Sun telescope, albeit much more weakly. Three slanted curves are shown, they are discussed in Sect. 3. The ion fluxes are highly variable throughout this particle event but, remarkably, the central pitch angle of the various telescopes does not change appreciably throughout most of the time period shown in Figs. 2 and 3. This time period is clearly enhanced in ^{3}He, its track is clearly visible in the two bottom panels of Fig. 2, especially early in the event in the SIS-A telescope, which points 30 degrees west of the Sun (see Table A.1). The fifth panel of Fig. 3 from the top shows bulk solar wind speed (solid black line), Alfvén speed (dotted black), thermal energy (in eV, red, right-hand axis), and density (blue, right-hand axis). The sixth panel from the top shows the T and N components of the solar

wind velocity. The N component (blue curve) increases steadily from $\sim -50\,\mathrm{km\,s^{-1}}$ around $\sim 12{:}00$ to slightly positive values around $\sim 00{:}00$ on 10 April, while V_T (black) sees a decrease from $\sim +50\,\mathrm{km\,s^{-1}}$ to $\sim -30\,\mathrm{km\,s^{-1}}$. The seventh panel shows the IMF R, T, and N components, and a thin horizontal dash-dotted line has been added to indicate 0 nT. The second panel from the bottom shows the color-coded power spectral density of the fluctuations in the IMF, as well as the proton gyro period in the solar wind rest frame (dashed blue line) and the period at which energetic protons are in first-order cyclotron resonance (solid blue line). The Alfvénic Mach number is plotted in black against the right-hand y-axis. The low level of fluctuations, low Mach number, and bidirectional electron streaming between the two thick dashed lines are signatures that indicate that Solar Orbiter was very likely embedded in an ICME during this time period, the slow rotation of the B_T component indicates that it was inside a flux-rope-like part of the ICME. The bottom panel shows the pitch-angle distribution of 70 eV electrons as provided by SWA/EAS. It shows clear bi-directional streaming throughout most of the time period studied here, but with some interruptions. Fortuitously, a large part of the solar particle event discussed here was observed during the calm period of low Alfvénic Mach number solar wind flow between 11:10 on 9 April (indicated by the thick vertical dashed line) and 00:00 on 10 April (thick vertical dashed line, also indicated by annotation a).

For ions, the particle event that we discuss in this paper is seen clearly in Figs. 2 and 3 in the north telescope and also in the Sun telescope, but not in the anti-Sun and south telescopes. The event is obviously strongly anisotropic and the range of pitch angles covered by the north telescopes is clearly smaller than for the other telescopes. The onset of the event appears at the highest energies ($\sim$6 MeV) around 13:30 and proceeds toward lower energies with increasing time. Starting around 00:00 on 10 April (annotation a) energetic particles are seen in all telescopes. Even at those late stages the event is still highly anisotropic, the differential fluxes are clearly different for the four telescopes.

The likely solar source region of this event can be identified in extreme ultraviolet at 174 Å collected by the Full Sun Imager of EUI as shown in Fig. 4 at 11:10:50, 11:30:50, 11:40:50, and 12:00:50 (on 9 April 2022, clockwise, starting from the upper-left panel). An eruption can clearly be seen at 11:30:50 (upper-right panel, indicated by a red arrow) at $\sim$55 degrees longitude and $\sim$17 degrees latitude (or helioprojective longitude $\sim$1800$''$ and helioprojective latitude of $\sim$700$''$). Coronal material can be seen escaping from the Sun on the western limb at 11:40:50 (also indicated by a red arrow). A narrow CME corresponding to this eruption was also seen by the Large Angle and Spectrometric Coronagraph Experiment (LASCO; Brueckner et al. 1995) on the Solar and Heliospheric Observatory (SOHO; Domingo et al. 1995) but is not shown here.

3. Analysis

To determine the time at which the ions or electrons were released at the Sun, we transform the information of measured energy to inverse speed of the particle. An example for ions (electrons) is shown in Figs. 5 and 6 for the north magnet (foil) channel, which detects ions (electrons; Rodríguez-Pacheco et al. 2020). In this representation, the lower boundary of the proton (electron) track seen in Fig. 3 appears at the upper edge of the ion (electron) tracks and is indicated by a series of circles and a straight line. The second, lower track in Fig. 5 is due to helium

particles, their inverse velocity is shown on the right-hand axis[2]. The points (empty circles connected by a red line) for protons and helium nuclei (electrons) were placed by eye at the locations of the earliest arriving particles by pointing and clicking on the computer screen. A straight line was fitted to these points, their intercept with the x-axis gives the solar release time, and the slope of the line is determined by the path length that the particles traveled. This procedure was repeated $n_{\mathrm{det}} = 16$ (9) times for the proton (helium, electron) track and all "point-and-click" values for one ion species were stored in a file resulting in N data points. Subsequently we randomly chose n points from this list of N values and again fitted a straight line to these points. The number n was chosen to be the average number of data points picked in the manual point-and-click procedure: $n = N/n_{\mathrm{det}}$, where $n \approx 40$. This randomized choice was repeated 1000 times to estimate the uncertainty of the determination of solar release time and path length. This procedure was repeated for electrons, protons, and helium nuclei for the telescopes in which an onset could be seen (i.e., the north and Sun telescopes for ions). The resulting distributions are generally close to a Gaussian profile as would be expected from such a random choice.

The results of these determinations are given in Table 1 where t_0 is the inferred solar release time, Δt_0 the corresponding standard deviation, s the path length traveled by the particles, and Δs the corresponding standard deviation. n_{det} gives the number of point-and-click determinations, α the pitch angle at 12:00 (for electrons) and 18:00 (for ions). The fact that we observe beams indicates that scattering only plays a minor role in the transport of the particles in this solar particle event. Nevertheless, the earliest particles to arrive will be those that have experienced the least scattering and are likely to lie on the edges of the FoVs that lie closest to the "beam center".

The upper half of Table 1 shows the results for protons and helium for the Sun and north telescopes. Inferred solar release times lie between 11:14 and 12:07, their uncertainties (formally the standard deviations of the procedure outlined above) are considerable. The p1 and p2 entries for the north telescope are for the two tracks seen in Fig. 3 and are further discussed in Sect. 4. The lower half of Table 1 shows the results for the two electron injections as determined by the same procedure as for ions and illustrated in Fig. 6. Inspection of Fig. 2 for all but the north telescope shows that the onset determination is difficult and that the uncertainties would be considerable. Electrons seen in these other three telescopes appear delayed compared to the two injections seen in the north telescope and the "fuzziness" of their onsets implies significant scattering. The two clear injections visible in the north telescope can be seen more clearly in Fig. 7, which is discussed in the following paragraph.

Figure 7 shows from top to bottom STIX light curves (generated from the spectrogram data product and re-binned to 4 s time resolution) for the X-ray energies given by the labels. Those for 4–10 keV and 10–15 keV are dominated by thermal emission, as shown by their rather gradual time evolution. In contrast, the higher-energy X-ray count rates in the second panel show the much more impulsive time profiles that are typical for the nonthermal component in solar flares. STIX times have been shifted by 215 s (indicated by a horizontal bar in the second panel from the top) to Solar Release Time (SRT), the

---

[2] Figure 5 makes use of raw data from EPT. If deposited energy is larger than the energy at which protons penetrate the detector, then it is assumed to be due to helium. This lower track is covered by the dots that indicate the "clicked points" but can be seen in Figs. 2 and 3, where it is indicated by a dashed line.
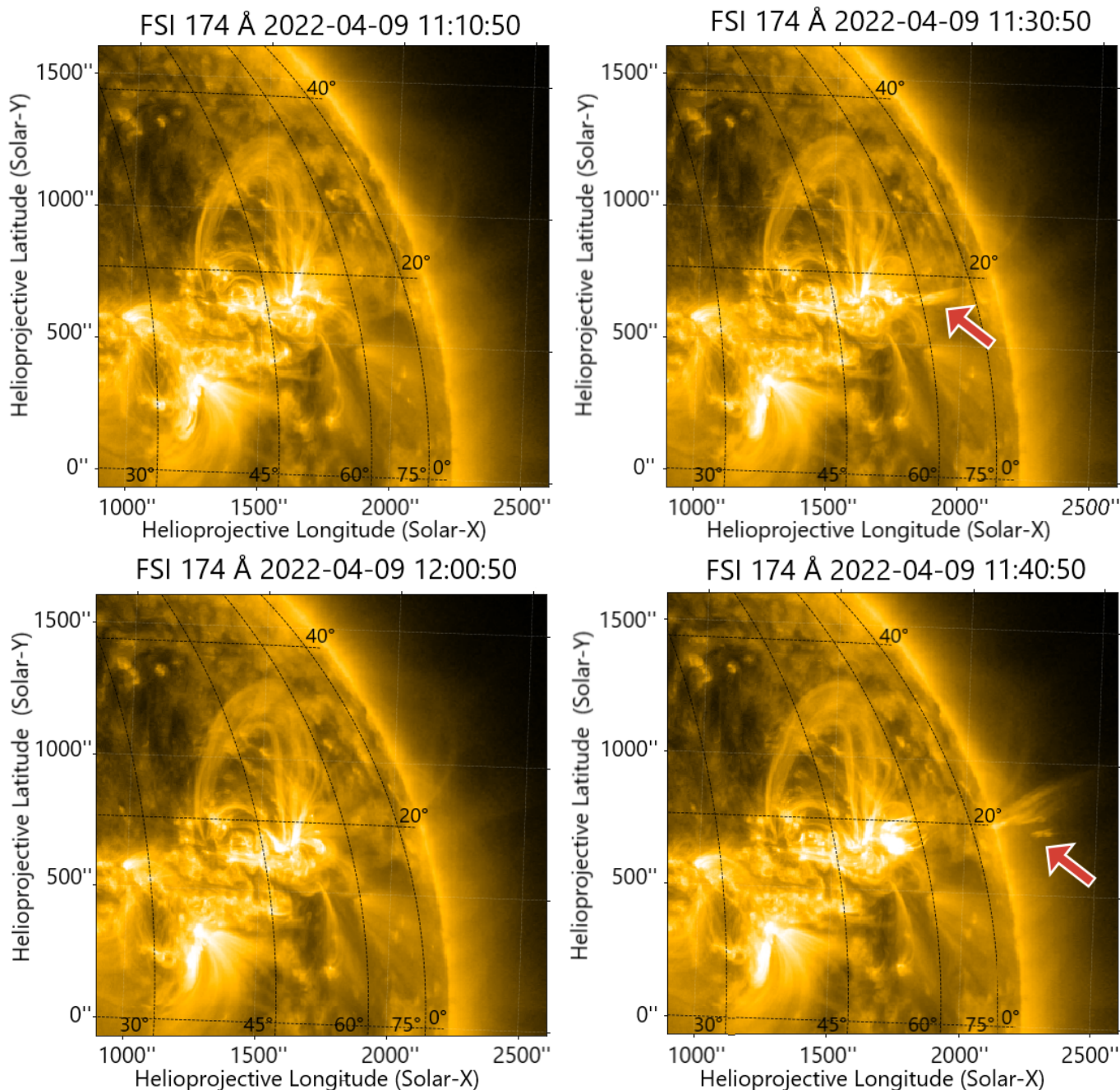
Fig. 4. EUI-FSI 174 Å images of the Sun for 9 April 2022. The individual panels show images at 11:10:50, 11:30:50, 11:40:50, and 12:00:50 (clockwise starting at the upper-left panel). The black grid shows the heliographic coordinates from the Solar Orbiter perspective. The eruption can be seen at 11:30:50 (upper-right panel) at ~55 degrees longitude and ~17 degrees latitude (or helioprojective longitude ~1800″ and helioprojective latitude of ~700″); it is marked with a red arrow. The ejecta can also be seen at 11:40:50 (bottom-right panel) and are indicated by a red arrow. Data are from EUI data release 6.0 2023-01, https://doi.org/10.24414/z818-4163.

gray light curve in panel 2 shows an un-shifted version of the 25–50 keV light curve (i.e., in measurement or spacecraft time). Panels labeled HET C, HET AB, and EPT show electron measurements from those co-aligned sensors as well as the VDA curves for both electron injections, which were determined as described above in the discussion of Fig. 6. The horizontal bars marked $s/c \approx 675$ s (in panel HET C) indicate the travel time of highly relativistic electrons along the IMF that was assumed to be the average of the IMF lengths for the two electron events, that is, $(1.231 + 1.456)/2 \approx 1.35$ au. The bottom panel shows the central pitch angle for the north telescope, which only varies by a

few degrees over the duration of the electron measurements (the variance of the 1 s-averaged pitch angle during this time period is 2.8 degrees). For comparison, we note that the half opening angle of an EPT telescope is 15 degrees. Times given for in situ measurements (EPD and MAG data) are measurement times at Solar Orbiter. Two flares are apparent in the STIX count rates shown in Fig. 7. The first is a smaller event occurring during the decay phase of a preceding larger flare. It is quite impulsive, peaks at 11:22:15, but barely shows any emission above 25 keV. The second event is much larger, with count rates starting to rise at 11:33:55 and peaking at 11:37. No corresponding GOES
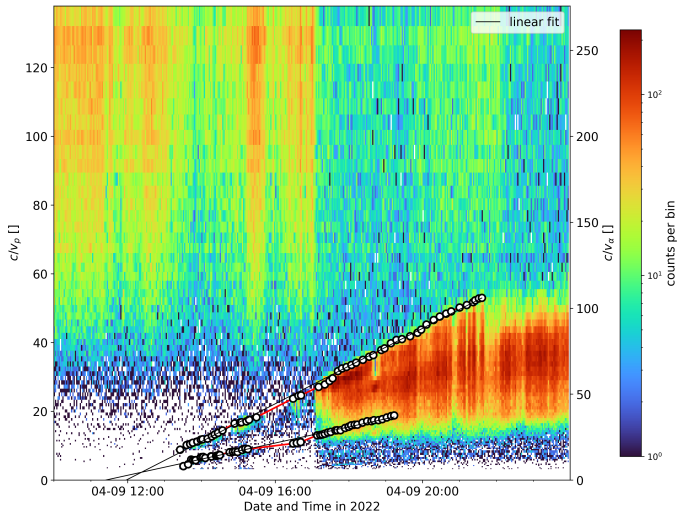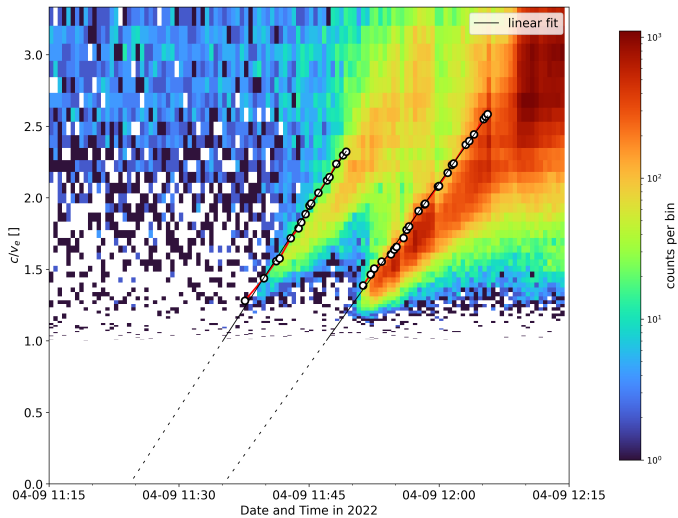
Fig. 5. EPT measurements from the magnet telescope plotted as inverse velocity (assuming that the particles are protons) vs. time. In this representation, ions that are released at the same time but have different velocities lie along a straight line. The upper curve shows "point-and-click" values for protons, the lower for helium nuclei as well as their linear fits. The left-hand y-axis is for protons, the right-hand y-axis for α particles. The changed path length around 18:40 (the "p2" track in Table 1) is also clearly visible.

Fig. 6. EPT measurements from the foil telescope plotted as inverse velocity (assuming that the particles are electrons) vs. time in the same format as Fig. 5. Two electron injections are clearly visible; their timing information is given in Table 1. Dashed lines extrapolate to the inferred solar release time.

measurements are available for these flares since they were both not visible from Earth. However, we can estimate a GOES class of M1 for the second event based on the 4–10 keV STIX count rate[3]. The first flare is contaminated by the decay of the larger previous event, so we can only roughly estimate it as a mid-B class flare. Focusing on the larger flare, the count rates above 25 keV show a very fast rise to the main nonthermal hard X-ray peak at 11:34:33, which is followed by three minor peaks during the following 90 s. This clearly implies several very impulsive

---

[3] https://datacenter.stix.i4ds.net/wiki/index.php?title=GOES_Flux_vs_STIX_counts

phases of electron acceleration to energies of at least 100 keV. Hard X-ray images provided by STIX (not shown here) reveal the classical scenario of two chromospheric nonthermal X-ray foot points visible at the higher energies that are connected by a thermal loop source in the corona.

The first electron event (1) is delayed by approximately three minutes with respect to the first, but very small peak in X-ray emission, as would be expected based on previous studies (Krucker et al. 1999; Haggerty & Roelof 2002; Simnett et al. 2002). Remarkably, the inferred solar release time of the second electron event (2) lies very close to the peak in 25–50 keV X-ray emission, and agrees with it within the estimated uncertainties given in Table 1.

4. Discussion

Figure 7 shows that Solar Orbiter observed two homologous X-ray flares that were only ~12 min apart. They are accompanied by radio emissions driven by the outward-propagating energetic electrons, which were also measured in situ but are not shown here. The two electron events are followed by an initially highly intermittent and focused ion beam that grows in intensity with time. To determine the angular width, σ, of the observed ion beam we make use of our knowledge of the direction of the IMF and assume that the pitch-angle distribution is symmetric around the IMF. For simplicity's sake, we assume a Gaussian angular profile. Then the intensity I_i seen in direction i is given by

$$I_i = \frac{I_0}{\sqrt{2\pi\sigma^2}} e^{-\frac{\delta_i^2}{2\sigma^2}}, \tag{1}$$

where δ_i is the pitch angle for telescope i and I_0 is the unknown intensity along the IMF (i.e., for zero degrees pitch angle). Taking the ratio of intensities in two different directions one easily solves for the width of the beam,

$$\sigma = \sqrt{\frac{\delta_i^2 - \delta_j^2}{2\ln(I_j/I_i)}}. \tag{2}$$

Reading off an ion intensity ratio of $I_{\rm sun}/I_{\rm north} \sim 0.1$ from Fig. 3 at 18:00 (annotation b) and the average pitch angles for the Sun and north telescopes from Table 1, we readily obtain a width of $\sigma \approx 28$ degrees, which is comparable with the full opening angle of the EPT telescopes of 30 degrees. Two points are worth noting here. First, we cannot verify this inferred angular width of the beam or obtain more precise directional information using data from the multi-pixel detector array of STEP (see Rodríguez-Pacheco et al. 2020 for an introduction to this sensor of EPD) because the beam was not seen at the much lower energies covered by STEP in the sunward direction. Second, the thus estimated width is highly uncertain because we used the nominal pointing directions of the two telescopes. This is valid for a (near-)isotropic distribution, but not in the highly an-isotropic event studied here.

That neither the anti-Sun nor the southward-pointing telescopes saw the beam indicates that it was propagating away from the Sun and that there was no appreciable pitch-angle scattering across 90 degrees until about 22:04 on 9 April, 2022, that is to say, about 10 h after the solar release time of the event (annotation c). Intriguingly the changes in the observed pitch angle are not larger at this time than some of the small fluctuations earlier on in the event. The most dramatic change appears just before 00:00 on 10 April (annotation a), when the Sun, anti-Sun, and
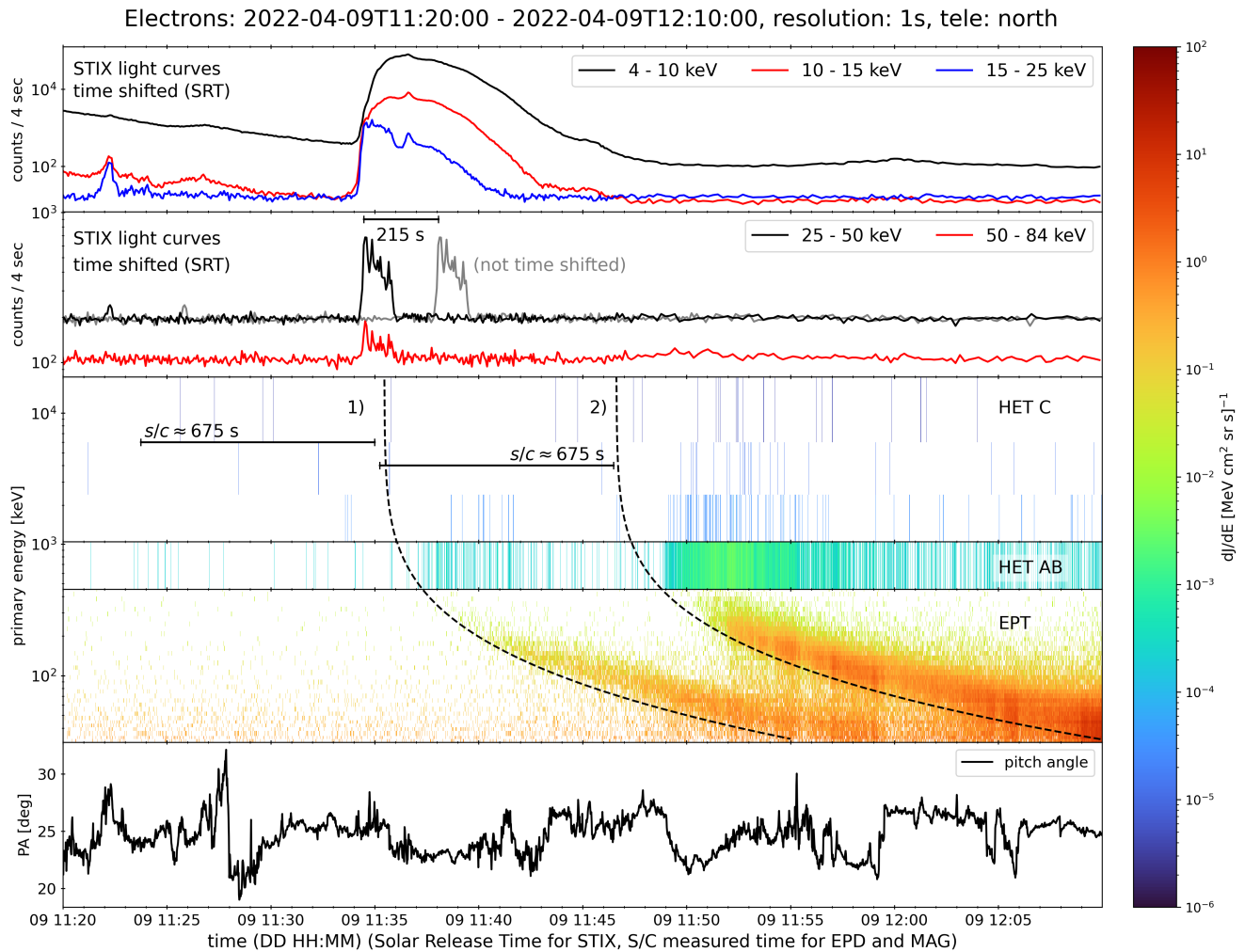
Fig. 7. STIX X-ray light curves and their interplanetary counterparts. Top two panels: STIX light curves for the X-ray energies indicated by the legends, time-shifted by 215 s, i.e., in Solar Release Time (SRT). The gray 25–50 keV curve has not been time-shifted. Third panel (HET C): Electrons measured in the HET BGO crystal. The threshold for detection lies above 1 MeV, so these measurements are clear indications of relativistic electrons. Fourth panel (HET AB): Coincidence measurements of the HET A and B detectors; their energy range lies between ∼500 keV and 900 keV. Fifth panel (EPT): Electrons measured by EPT. See the main text for a discussion. Bottom panel: Central pitch angle covered by the EPD north telescopes. Note the narrow range of the *y*-axis. All in situ times are measurement times at Solar Orbiter. Dashed velocity dispersion curves are shown for the two electron injections, (1) and (2), as discussed in the text. Horizontal black bars in the third panel from the top (HET C) indicate the time shift for highly relativistic electrons based on the fitted length of the IMF (675 s); we used the average (1.35 au) of the two determinations given in the electron rows of Table 1.

southward telescopes saw approximately the same intensities (within a factor of ∼4), all of which were at least ten times lower than those seen by the north telescope. A similar, but much less pronounced, change occurred around 22:22 on 9 April (annotation d). The anisotropic "beam" of ions disappears around 03:00 on 10 April 2022 when all telescopes see similar fluxes because they all cover similar pitch angles. Anisotropy increases again around 05:00 on 10 April. We can thus state that the period of prolonged anisotropy persisted for more than 16 h.

After the vertical dashed line in Fig. 3 at 11:10 the level of fluctuations in solar wind properties is low and it is straight-forward to calculate the Alfvén speed throughout this interesting time period. One finds a value of ∼120 km s^{-1}, which is a substantial fraction of the low solar wind speed of ∼300 km s^{-1} measured throughout this time period. This results in an unusu-ally low Alfvénic Mach number for the solar wind. Alfvén speed has also been plotted as a dotted line in panel 5 of Fig. 3. The solar wind is obviously still super-Alfvénic, but

with a low Alfvén Mach number, as is indicated in panel 8 in Fig. 3.

An intriguing feature appears around 17:06 on 9 April (anno-tation e) when the scatter-free proton beam appears to widen toward higher energies. Assuming that these higher-energy pro-tons were released at the same time as the scatter-free beam implies that these protons must have undergone significant scat-tering, which in itself is not unusual. The remarkable feature appears about half an hour later when the widened proton beam appears to split into two beams, one at higher energies, one con-tinuing along the original dispersion track. Moreover, all ion (protons and helium) tracks are shifted to higher energies around 18:37 and back to the lower energies of the original track around 18:52 (annotation f). This behavior is seen in both the north and Sun telescope. Close inspection of Fig. 3 around this time shows that the two proton beams appear to coexist before and after this brief period when the primary beam appears to be shifted toward higher energies by approximately 40%. The same relative energy

Table 1. Properties of the 9 April 2022 solar particle event.

Ions	t_0	Δt_0 [MM:SS]	s [au]	Δs [au]	n_{det}	α at 18:00
Sun, p	11:14:29	05:50	2.103	0.03	12	67
Sun, 4He	11:35:02	14:32	1.986	0.075	12	67
North, p1	11:45:16	02:58	1.374	0.011	16	29
North, p2	12:06:53	05:16	1.678	0.021	11	29
North, 4He	11:31:38	04:14	1.523	0.022	9	29
North 3He	11:40:59	05:08	1.675	0.03	12	29
Electrons						α at 12:00
North, e1	11:25:14	00:33	1.231	0.038	9	25
North, e2	11:34:29	00:28	1.456	0.028	9	25

Notes. Times are given in UT. See the main text for a discussion. Individual columns are: t_0 inferred solar release times, s path lengths, α central pitch angle of the Sun and north telescopes at 18:00 and 12:00. Results for ions are shown in the upper half, results for electrons in the lower half.

increase is seen in the Sun telescope. The orientation of the IMF, and hence the pitch angle do not change appreciably during this time period, solar wind velocity, temperature, and density only undergo very small changes and not all of them are correlated with changes in the proton beam. The solar release time inferred from VDA for this "parallel track" is approximately 10 min later than that of the first and more prominent track and is labeled "p2" in Table 1. The inferred IMF length for p2 is longer than for p1, which is puzzling because both tracks are seen at the same time and in the same flux tube. This most probably illustrates the uncertainty of the determination of the onsets for the VDA of this proton track, the p2 track must be picked out against a higher background than p1. While it is tempting, we cannot, based on the available data, decide whether these two proton beams (p1 and p2) correspond one-to-one to the two electron injections, e1 and e2. Starting on 10 April, the event in ions is clearly seen in all telescopes, especially also at pitch angles for particles streaming back toward the Sun.

An important factor contributing to the unique properties of this event is certainly that it is associated with an ICME, mainly with the flux-rope part of it. It is well known that the level of IMF fluctuations inside ICMEs is low (Wimmer-Schweingruber et al. 2006), which would explain why the ions and electrons retained their narrow pitch-angle distribution despite the long path length. The low level of fluctuations of the IMF is clearly seen in Fig. 3, which also shows bi-directional 70 eV electrons that provide evidence that the flux rope is connected back to the Sun by both ends most of the time (i.e., when bi-directional electrons are seen). Nevertheless, this scenario begs the question of how the IMF would remain so constant throughout the event. Small-scale flux dropouts align well with discontinuities seen in the bi-directional electrons, as is exemplified by the dotted vertical lines. Some, but not all dropouts have been indicated by dotted vertical lines in Figs. 2 and 3[4]. As already observed by, for example, Mazur et al. (2000) and more recently Ho et al. (2022), intensity dropouts and rebounds are observed at all times but are not always accompanied by a discernible change in pitch angle.

5. Interpretation

Our observations are reminiscent of those of Torsti et al. (2004) who investigated the 2–3 May 1998 ICME and found that the particle intensities in the field-parallel direction were ∼1000 times higher than in the perpendicular direction during

the ICME. They found a parallel mean free path of at least 10 au and termed this the interplanetary "highway" for SEPs. Contrary to the long duration of the anisotropy reported here, they observed counter-streaming ions within 30–45 min after the onset. Using data from the Wind Three-Dimensional Plasma and Energetic Particle Investigation (3DP) Solid-State Telescope (SST) and the Energetic Particles: Acceleration, Composition, and Transport (EPACT) Low Energy Matrix Telescope (LEMT), Tan et al. (2013) investigated electron and ion data during ground-level enhancements and found that the path lengths along which electrons and ions propagate agree to within ±10%. They found that the observed path length consistency implies that the maximum stable time of magnetic flux tubes, along which particles transport, could reach 4.8 h. This is considerably shorter than the time observed for this 9 April 2022 event at 0.43 au. On the other hand, using the Low Energy Telescope (LET) in STEREO-A Leske et al. (2012) found large bidirectional anisotropies in 4–6 MeV protons for the first ∼17 h of the 18 August 2010 event while inside a magnetic cloud, with intensities along the field direction several hundred to nearly 1000 times greater than those perpendicular to the field. Using VDA, those authors found an enhanced path length of 1.7 au along which the particles had traveled; this is longer than the typical 1.2 au. The unusually long magnetic connection back to the Sun reported here is comparable to that reported by Gómez-Herrero et al. (2017), who studied two interacting ICMEs with SEPT on STEREO. They found effective electron propagation path lengths of 2.9 and 3.5 au, which are distances about three times longer than a nominal magnetic connection back to the Sun, similar to the event presented here. We note, however, that the IMF in the 9 April 2022 event studied here shows only very small and slow variations throughout the event, which limits the possible number of field-line rotations to <1 for the flux-rope part of the ICME visible at Solar Orbiter.

The solar electron and ion events reported here are unusual not only because of their long field line, but also because the timing of these two homologous pairs of (electron and ion) events appears to agree well with the X-ray observations. In their seminal study Krucker & Lin (2000) investigated 26 solar energetic proton events with clear velocity dispersion observed by Wind and found that there were two classes. The 18 class-1 events showed normal path lengths of 1.1–1.3 au while the 8 class-2 events showed larger path lengths around 2 au. For all 26 protons events the associated electrons showed path lengths of 1.1–1.3 au. In their class-1 events protons are injected ∼0.5−2 h after the electrons. These authors attributed the late injection of protons to them being accelerated by a coronal shock roughly 1–10

---

[4] Not all have been indicated in order not to crowd the figure even more.

solar radii above the site of electron acceleration. They interpreted the apparent longer path length of the protons in the class-2 events as due to a successively later solar release of protons at successively lower energies, which would mimic a longer path. They considered transport processes an unlikely reason because the protons in their study arrived nearly scatter free. Their results for electrons were confirmed independently by Simnett et al. (2002) and Haggerty & Roelof (2002) who also found that the electrons measured in situ are generally released later (∼10 min) than the electrons which are responsible for the X-ray and radio emission. The 9 April 2022 event discussed in this paper, however, shows very similar path lengths and injection times for electrons and ions which are also in reasonable agreement with the timing of the X-ray flares. While the ions are injected after the electrons in this event, the time lag is small compared to the Krucker & Lin (2000) results, especially if the ions were accelerated in conjunction with the second, more energetic flare or electron acceleration event.

We end this section by noting that the uncertainties given in Table 1 are statistical only, as discussed above. Because the point-and-click method was performed by a human being, a certain bias was introduced. To assess this bias, we performed the following test. We assumed that the ions were released at the same time as the X-ray flare and that they had to travel along a path length of 1.4 au and compared the resulting velocity dispersion with the observations and found good agreement. Thus, we can say that the ion (and electron) release times are consistent with the timing of the X-ray flares and that the path lengths found using VDA agree well with this comparison. While the exact timings may be uncertain to within a few minutes, the key result, that ions and electrons traveled virtually scatter-free along an unusually long field line, is robust.

6. Conclusions

We have reported observations of a nearly scatter-free solar particle event with an unusually long connection back to the Sun. While the spacecraft was at 0.43 au, the inferred IMF path length was approximately three times longer than the nominal Parker spiral length. Despite this long path length, electrons and ions are observed as a beam with a $1/\sqrt{e}$ angular width of ∼30 degrees and with very narrow energy distributions. Variations in pitch angle are small throughout the event, but significant variations in intensity (dropouts) are observed at all temporal scales. Given that the beam width is much larger than the observed angular changes in the IMF, the large intensity changes for small directional changes imply that individual flux tubes are connected to different locations at the solar source, where they are filled with energetic particles to varying degrees.

Remarkably, the IMF pointed in the negative N direction (in Radial, Tangential, Normal (RTN) coordinates) throughout the event, an unusual orientation, and particles were observed primarily by the EPT north telescope. This unusual orientation, likely due to Solar Orbiter being immersed inside an ICME flux rope, provided the unusually long path length along which the particles traveled. Furthermore, it limits the effect of (local) adiabatic focusing on the beam because the IMF is convected out radially without the possibility of expanding radially, as is normally observed in the inner heliosphere. Solar Orbiter was within 10 degrees of the ecliptic plane during the period reported here. The low level of fluctuations in the IMF throughout this time period resulted in less scattering than is usually observed and thus maintained the strongly focused electron and ion beams. Together, these observations provide strong limitations on the

properties of energetic particle transport inside an ICME (and the associated flux rope).

References

Brueckner, G. E., Howard, R. A., Koomen, M. J., et al. 1995, Sol. Phys., 162, 357
Domingo, V., Fleck, B., & Poland, A. I. 1995, Sol. Phys., 162, 1
Gieseler, J., Dresing, N., Palmroos, C., et al. 2023, Front. Astron. Space Sci., 9, 1058810
Gómez-Herrero, R., Dresing, N., Klassen, A., et al. 2017, ApJ, 840, 85
Haggerty, D. K., & Roelof, E. C. 2002, ApJ, 579, 841
Ho, G. C., Mason, G. M., Allen, R. C., et al. 2022, Front. Astron. Space Sci., 9, 939799
Horbury, T. S., O'Brien, H., Carrasco Blazquez, I., et al. 2020, A&A, 642, A9
Kaiser, M. L., Kucera, T. A., Davila, J. M., et al. 2008, Space. Sci. Rev., 136, 5
Krucker, S., & Lin, R. P. 2000, ApJ, 542, L61
Krucker, S., Larson, D. E., Lin, R. P., & Thompson, B. J. 1999, ApJ, 519, 864
Krucker, S., Hurford, G. J., Grimm, O., et al. 2020, A&A, 642, A15
Laitinen, T., & Dalla, S. 2019, ApJ, 887, 222
Laitinen, T., Huttunen-Heikinmaa, K., Valtonen, E., & Dalla, S. 2015, ApJ, 806, 114
Leske, R. A., Cohen, C. M. S., Mewaldt, R. A., et al. 2012, Sol. Phys., 281, 301
Mazur, J. E., Mason, G. M., Dwyer, J. R., et al. 2000, ApJ, 532, L79
Müller, D., St. Cyr, O. C., & Zouganelis, I. 2020, A&A, 642, A1
Müller-Mellin, R., Böttcher, S., Falenski, J., et al. 2008, Space. Sci. Rev., 136, 363
Owen, C. J., Bruno, R., Livi, S., et al. 2020, A&A, 642, A16
Reames, D. V., & Stone, R. G. 1986, ApJ, 308, 902
Reames, D. V., von Rosenvinge, T. T., & Lin, R. P. 1985, ApJ, 292, 716
Rochus, P., Auchère, F., Berghmans, D., et al. 2020, A&A, 642, A8
Rodríguez-Pacheco, J., Wimmer-Schweingruber, R. F., Mason, G. M., et al. 2020, A&A, 642, A7
Simnett, G. M., Roelof, E. C., & Haggerty, D. K. 2002, ApJ, 579, 854
Tan, L. C., Malandraki, O. E., Reames, D. V., et al. 2013, ApJ, 768, 68
Torsti, J., Riihonen, E., & Kocharov, L. 2004, ApJ, 600, L83
van den Berg, J., Strauss, D. T., & Effenberger, F. 2020, Space. Sci. Rev., 216, 146
Wang, L., Lin, R. P., Krucker, S., & Mason, G. M. 2012, ApJ, 759, 69
Wimmer-Schweingruber, R. F., Crooker, N. U., Balogh, A., et al. 2006, Space. Sci. Rev., 123, 177
Wimmer-Schweingruber, R. F., Janitzek, N. P., Pacheco, D., et al. 2021, A&A, 656, A22
Zhao, L., Li, G., Zhang, M., et al. 2019, ApJ, 878, 107

Appendix A: Pointing directions of the EPD sensors

It has come to our attention that the pointing directions of the individual EPD sensor's FoVs were not given in the EPD instrument paper (Rodríguez-Pacheco et al. 2020). We therefore give them here in Table A.1.

Table A.1. Central FoV pointing directions of the EPD sensors.

sensor	direction	ϑ [°]	φ [°]
STEP	Sun	0	35
STEP	pixel 1	-18.4	-27.6
STEP	pixel 2	-9.4	-27.6
STEP	pixel 3	0.0	-27.6
STEP	pixel 4	9.4	-27.6
STEP	pixel 5	18.4	-27.6
STEP	pixel 6	-18.4	-35.0
STEP	pixel 7	-9.4	-35.0
STEP	pixel 8	0.0	-35.0
STEP	pixel 9	9.4	-35.0
STEP	pixel 10	18.4	-35.0
STEP	pixel 11	-18.4	-42.4
STEP	pixel 12	-9.4	-42.4
STEP	pixel 13	0.0	-42.4
STEP	pixel 14	9.4	-42.4
STEP	pixel 15	18.4	-42.4
SIS	Sun	0	30
SIS	anti-Sun	0	160
EPT	Sun	0	35
EPT	anti-Sun	0	145
EPT	north	56.2	-122.5
EPT	south	-55.6	57.5
HET	Sun	0	35
HET	anti-Sun	0	145
HET	north	56.2	-122.5
HET	south	-55.6	57.5

Notes. For STEP, the centers of the individual pixels are also given. ϑ is the polar angle and φ the longitudinal angle; both are measured in the spacecraft RTN coordinate system.